Journal of Agricultural Engineering

https://www.agroengineering.org/

Development and validation of a low-cost imaging system for seedling germination kinetics through time-cumulative analysis

Marco Davide Michel Torrente, Alessia Follador, Aldo Calcante,

Paola Casati, Roberto Oberti

Department of Agricultural and Environmental Sciences - Production, Landscape, Agroenergy, University of Milan, Italy

Corresponding author: Aldo Calcante, Department of Agricultural and Environmental Sciences - Production, Landscape, Agroenergy, University of Milan, Via G. Celoria 2, 20133 Milan, Italy. E-mail: aldo.calcante@unimi.it

Please cite this article as doi: 10.4081/jae.2026.2130

Submitted: 3 November2025
Accepted: 17 July 2026

Development and validation of a low-cost imaging system for seedling germination kinetics through time-cumulative analysis

Marco Davide Michel Torrente, Alessia Follador, Aldo Calcante,
Paola Casati, Roberto Oberti

Department of Agricultural and Environmental Sciences - Production, Landscape, Agroenergy, University of Milan, Italy

Corresponding author: Aldo Calcante, Department of Agricultural and Environmental Sciences - Production, Landscape, Agroenergy, University of Milan, Via G. Celoria 2, 20133 Milan, Italy. E-mail: aldo.calcante@unimi.it

Authors' contributions: Marco Davide Michel Torrente, investigation, data curation, software, validation, writing - original draft. **Alessia Follador**, investigation, data curation, validation. **Aldo Calcante,** methodology, data curation, writing - review and editing. **Paola Casati,** conceptualization, resources, writing - review and editing. **Roberto Oberti,** Conceptualization, methodology, software, writing - review and editing.

Conflict of interests: the authors declare no potential conflict of interest and all authors confirm accuracy.

Availability of data and material: data and materials are available from the corresponding author upon request.

Funding: this study was carried out within the Agritech National Research Center and received funding from the European Union Next-GenerationEU (Piano Nazionale di Ripresa e Resilienza (PNRR) – Missione 4, Componente 2, Investimento 1.4 – D.D. 1032 17/06/2022, CN00000022).

This manuscript reflects only the authors' views and opinions, neither the European Union nor the European Commission can be considered responsible for them.

Abstract

The ready-to-eat lettuce industry is rapidly expanding, increasing the need for reliable, scalable methods to assess seed germination and early growth under realistic soil conditions. This study presents an automated imaging-based approach for quantifying germination

dynamics and seedling vigor using a low-cost multi-camera system under greenhouse conditions. Lettuce seeds were grown in soil either inoculated or non-inoculated with the soil-borne pathogen *Rhizoctonia solani*. Top-view images were acquired using commercial surveillance cameras and processed through a calibrated pipeline including geometric correction, color normalization, vegetation segmentation, clustering, and temporal tracking of emergence events. Seedling vigor was quantified through projected leaf area estimation. The proposed method enables accurate estimation of germination kinetics and growth dynamics under field-like conditions. Automated counts were validated against manual measurements at both intermediate and final time points, achieving high agreement in both cases. At the final assessment, the method reached $R^2 = 0.98$ and RMSE = 1.12, while at the midterm evaluation it achieved improved performance with $R^2 = 0.998$ and RMSE = 0.5, reflecting the lower complexity of plant structure at earlier growth stages. Results showed that pathogen inoculation significantly reduced both germination rate and seedling vigor, with up to 70% reduction in biomass accumulation. The proposed framework provides a robust, low-cost solution for high-throughput phenotyping of early plant development in soil-based systems, supporting scalable agricultural experimentation.

Key words: temporally-integrated imaging; germination; rhizoctonia; seedlings; biomass.

Introduction

The ready-to-eat produce industry has been one of the most rapidly expanding sector in the last decade within the fruit and vegetable market (Gullino *et al.,* 2019; Losio *et al.,* 2015). Lettuce (*Lactuca sativa L.*), a member of the Asteraceae family, is one of the most widely consumed salad crops worldwide. The growing demand for these products is driven by their convenience, consistent quality, and the increasing awareness of the link between health and the consumption of fresh vegetables (Tomasi *et al.,* 2015). Given its broad adaptability and widespread cultivation, lettuce is vulnerable to a range of diseases caused by fungi, bacteria, viruses, and nematodes (Raid and Sandoya-Miranda, 2024). Among these pathogens, *Rhizoctonia solani* is recognized as a soil-borne fungal pathogen with a broad host range, and as a major pathogen affecting both protected and open-field lettuce crops (Wareing *et al.,* 1986, Gonzalez Garcia *et al.,* 2006; Verwaaijen *et al.,* 2017). *R. solani* is responsible for seedling blight, decay, root rot, and a marked reduction of seeds germination, plant density,

vigor and yield of surviving plants. It also infects other important crops, including *Oryza sativa L.* (Kumar *et al.,* 2011), *Solanum tuberosum L.* (Daami-Remadi *et al.,* 2008), *Vicia lens L.* (Chang *et al.,* 2008), *Brassica napus L.* (Hwang *et al.,* 2014), *Zea mays L.*, where it affects root development and shoot growth (da Silva *et al.,* 2017).

To quantify the negative effects of soil-borne pathogens, or conversely to assess the beneficial effects of treatments applied in crop-protection trials, the dynamics of seed germination represents key feature. This parameter is evaluated with a manual counting during the experiment, with the aim of determining the percentage of seeds germinated at specific time points (Kumar *et al.,* 2011).

Another essential indicator to evaluate seeds vitality is the seedlings vigor, which relates to the rate of biomass accumulation and thus with leaf area development. To this aim, non-destructive measurement methods based on top-view images have significantly improved the accuracy of *in vivo* leaf area estimation in vegetable seedlings (Chien and Lin, 2005), whereas destructive methods rely on measuring the dry weight of the plant's aerial biomass (Anandan *et al.,* 2020).

Nevertheless, large-scale germination assessment experiments still commonly rely on human observation, resulting labor intensive and prone to observer errors, constraining the frequency, scale and accuracy of such experiments and finally highlighting the need of automated methods (Colmer *et al.,* 2020).

In recent years, automated seedling counting and germination vigor analysis have become increasingly important in agricultural research and seed testing, leading to the development of several dedicated systems. For instance, SeedGerm integrates both hardware and software components for automated seed imaging and machine learning–based phenotyping across multiple crop species (Colmer *et al*., 2020). While this system demonstrates high accuracy in seed counting and germination assessment, it is designed for controlled laboratory conditions, where seeds are placed on plates rather than in soil. Although this setup simplifies image analysis and counting, it does not fully represent real field-like conditions where seeds are sown in natural substrate.

The aim of this work is to automatically characterize the germination kinetics and growth vigor of lettuce plants using imaging techniques and a low-cost camera system. An additional objective is to perform the experiment under conditions as close as possible to those encountered in the field, where seeds are sown in soil. This approach ensures a more

representative evaluation, as potential treatments can also interact with the growth substrate. As a case study for validation of the method, seedlings were exposed to the soil-borne pathogen *Rhizoctonia solani C.* which was incorporated in the growth substrate, with the goal of adversely affecting germination and seedling vigor during early vegetative stages (Aydin, 2022). The automated method proposed in this study enables repeated counting of emerged seedlings throughout the experiment. In addition, at each counting stage, seedling vigor is quantitatively assessed by measuring the leaf area extracted from top-view images.

Materials and Methods

Inoculum preparation and application

The soil-borne fungal pathogen *Rhizoctonia solani* (Cooke) Wint, strain RS1, used in this study was isolated from millet (*Pennisetum glaucum L.*) kernels. The isolate was maintained on potato dextrose agar (PDA, Difco™) at 20°C and stored at 4°C. To prepare the inoculum, three 1 cm^2 blocks of actively growing *Rhizoctonia solani* mycelium were added to a flask containing 200 g of pearl millet previously autoclaved (twice at 121°C for 30 min with 100 ml of water). The inoculated flask was incubated for three weeks at 20°C. The grown mycelium was then separated and dried at 30 °C until complete desiccation and then the resulting inoculum was incorporated into the soil at a concentration of 4 g kg^{-1} one week before sowing.

Experimental setup

Lettuce plants were cultivated in a greenhouse at the Department of Agricultural and Environmental Sciences of the University of Milan (Italy) under controlled conditions at 24/20°C day/night temperature, with 60-75% relative humidity and 16 h photoperiod.

Six replicates were treated with the inoculum and an equal number of non-inoculated controls were prepared. Each replicate consisted of a 17 x 17 cm pot (*p*) in which 49 baby lettuce seeds were sown on 2 x 2 cm grid in 100g of commercial sowing substrate (Vigorplant® Completo® pH [H_2O] 6÷7 EC 0.3÷0.4 dSm^{-1}). Each test lasted 10 days from the seed sowing until harvesting. Colour imaging of plants was carried out by threeTP-Link Tapo C-310 cameras (res. 1296 x 2304 pixels) installed above a workbench measuring 1 m x 0.8 m. The imaging system is based on a 1/2.8" progressive scan CMOS sensor equipped with a 3.9 mm focal length lens (F2.0 aperture), providing a field of view of 84° (horizontal), 46°

(vertical), and 100° (diagonal), according to manufacturer specifications. The cameras (*c*) were positioned at a height of 0.8 m from the workbench surface, allowing full monitoring of the experimental area with sufficient image resolution. With this configuration each camera captured images of four pots, for a total of 12 pots monitored simultaneously. The cameras were arranged to provide non-overlapping spatial coverage of the experimental area, ensuring that each pot was observed by a single dedicated camera throughout the experiment. This setup ensured consistent and parallel observation of inoculated and control groups under identical environmental conditions.

The cameras were programmed to record five one-minute video sequences per day at three-hour intervals from 08:00 a.m. to 08:00 p.m. The experimental time (*t*) was expressed as the number of hours elapsed since sowing.. The images analyzed in this study are single frames extracted from compressed video streams. Since the acquired frames exhibited reduced quality due to compression artifacts, a series of image pre-processing operations was applied prior to analysis. These included de-noising, sharpening, and contrast enhancement, aimed at improving the visibility of plant structures and ensuring reliable downstream segmentation.

Validation of automated counting *via* manual assessment

Validation of automated counting was performed through manual assessment at two time points: a midterm evaluation at 96 h and a final evaluation at the end of the experiment (192 h). The manually obtained counts were compared with the automated results obtained from the analysis of the last image acquired by each camera. This specific time point was selected for validation as it represents the most challenging phase for image-based quantification, due to the advanced seedlings growth and the formation of dense clusters that hinder accurate segmentation of individual plants.

Imaging system calibration

The image analysis calibration procedure consisted of four main steps: i) correction of the barrel distortion introduced by the wide angle lens in the raw images; ii) determination of the area within each camera's field of view corresponding to a specific pot; iii) identification of reference markers for automatic centering and color normalization; and (iv) evaluation of the conversion factor between pixels and physical size units.

The geometric calibration aimed to correct lens-induced barrel distortion. This was achieved through image rectification using a dedicated undistort functions available in MATLAB (R2023b; The MathWorks, Natick, Massachusetts). The geometric calibration requires the estimation of accurate camera parameters, which was achieved by acquiring 20 images of a checkerboard pattern. These images were then used to estimate both intrinsic and extrinsic camera parameters following the method proposed by Zhang (2000).To determine the fixed area corresponding to each specific pot within the field of view of each camera, an image was acquired after positioning the pots in their fixed experimental layout and placing a standard visual marker (*AprilTags*) of identical size to each single pot. AprilTags are graphical fiducial markers commonly used in automation and robotics applications to determine the size, position and identity of tagged objects (Olson, 2011). The use of these markers offers the advantage of automatic detection through dedicated functions, such as *readAprilTag,* in MATLAB environment. Following geometric correction, the calibration images were analyzed to detect the AprilTags identifying individual pots. The vertex coordinates of the detected markers were then used to generate corresponding polygons, which were subsequently converted into binary masks ($MaskR_{(p)}$) using the *poly2mask* function. These masks were later applied during the analysis phase to isolate and segment the individual pots, the vertex coordinates of the detected markers were used to generate corresponding polygons, which were subsequently converted into binary masks using the *poly2mask* function. For each camera, an additional AprilTag was positioned at the centre of the field of view and remained fixed throughout the experiment to facilitate the temporal alignment of images. This reference marker allowed to compensate for slight camera shifts, thereby ensuring frame-to-frame comparability acquired at different time points. Furthermore, the central marker enabled the automatic localization of a gray reference, which was permanently included in the field of view and used for color normalization across different acquisition times. Since the reference surface was achromatic, qual target values were assigned to the three color channels. The RGB target value was set to [155, 155, 155] ($Gray_{(R,G,B)}$) corresponding to a mid-range intensity level within the 8-bit scale, selected to avoid saturation and minimize noise amplification during normalization.To determining the spatial conversion factor between pixels and the corresponding surface area, given the known dimensions of the markers, this parameter ($KConv_{(c)}$) was estimated for each camera by dividing the actual marker area by the number of segmented pixels within the

corresponding mask for each pot. The resulting values were then averaged across replicates for each camera. This conversion factor was subsequently employed in both the distance-based clustering process described below (section "Clusterization and counting"), and in the estimation of leaf area for assessing seedling vegetative vigor, as detailed in the successive section "Growth vigor".

Data processing

Color normalization

The normalization of color channels across images acquired at different experimental time points was performed by sampling a 10×10 pix region of interest (ROI) from the central area of the gray reference to calculate the mean intensity values for the red, green, and blue channels ($Mean_{(R,G,B)}$). These values were then compared with the predefined reference gray value ($Gray_{(R,G,B)}$) to compute a normalization coefficient for each channel. The resulting coefficients, which reflect the lighting conditions at the time of image acquisition, were applied to normalize the color channels across different time points, as described in Eq. 1.

$$INorm_{(R,G,B)} = \frac{Gray_{(R,G,B)}}{Mean_{(R,G,B)}} \cdot I_{(R,G,B)} \quad \text{(Eq. 1)}$$

where $INorm_{(R,G,B)}$ is the normalized intensity of each RGB channel, $I_{(R,G,B)}$ is the original intensity of the image, $Mean_{(R,G,B)}$ represents the mean intensity of the gray reference region of interest for each channel, and $Gray_{(R,G,B)}$ is the predefined target gray reference value used for normalization.

Image analysis

The next stage of processing involved the segmentation of emerged plants, the assignment of each plant to its corresponding pot (e.g. individual replicates), and clustering of elements within each pot based on proximity to generate polygons of single or aggregated plants.

To this end, the first step focused on improving edge definition by applying the *imsharpen* function in MATLAB. This operation, based on unsharp masking, was applied to the full RGB image in order to enhance structural boundaries across all channels prior to channel selection. Although vegetation segmentation was ultimately performed on the green channel, applying sharpening at the RGB level allows edge enhancement to exploit the full luminance information contained in the image, improving boundary definition under variable

illumination and compression artifacts. Following this step, the green channel was extracted for gradient computation, as it maximizes the contrast between plant tissue and soil background.

Following the sharpening, image edges are more accurately detected by computing the gradient using the Sobel method (implemented via the specific function *imgradient*). In this process, only the green channel of the image is analyzed, as it maximizes the contrast between the green plant tissue and soil background. A threshold was then applied to the gradient matrix, determined using Otsu's method, to exclude pixels with gradient values above this threshold. It is important to note that the Sobel-based gradient thresholding is not directly used to define the final segmented regions, but rather to enhance edge information and suppress high-gradient boundary pixels prior to vegetation extraction. The actual segmentation of plant regions is subsequently performed using the Excess Green index (ExG) thresholding combined with the pot-specific region mask. This procedure produced a binary mask in which distinct blobs correspond to regions of relatively uniform green coloration. To further refine the results, a minimum size filter of 25 pix. (equivalent to 4.75 mm^2) was applied to remove noise particularly due to background elements erroneously segmented. Subsequently, the segmentation is predominantly green. This was achieved by calculating the excess-green vegetation index (*ExG*) (*Eq. 2*) for each single pixel and imposing a minimum threshold to select green areas.

$$ExG = 2G - R - B \quad \text{(Eq. 2)}$$

where (ExG) is the excess green vegetation index, and (R), (G), and (B) represent the red, green, and blue channel intensities of the image, respectively.

The threshold was determined using Otsu's method on a subset of sample images randomly extracted from the experiment, yielding to a threshold value of $T_{ExG} = 25$ which aligns with other examples found in the literature (Patrignani and Ochsner, 2015). This value was then applied to all the images acquired across the experimental database to segment vegetation, i.e. green pixels (Eq.3):

$$GreenP_{(p)} = \left[\left(ExG > T_{ExG}\right)\right] AND \left[MaskR_{(p)}\right] \quad \text{(Eq. 3)}$$

where $GreenP_{(p)}$ is the binary vegetation mask for pot (p), ExG is the excess green index value for each pixel, T_{ExG} is the threshold value determined using Otsu's method and $MaskR_{(p)}$ is the region-of-interest mask defining the spatial extent of pot (p). The logical AND operator ensures that only pixels classified as vegetation within the pot area are retained.

Growth vigor

For each camera (*c*) the estimation of the vegetative vigor for an individual pot, denoted as $LeafArea_{(c,p,t)}$, is based on the evaluation of the projected leaf area of the emerged seedlings. This value was obtained by multiplying the spatial conversion coefficient of each camera ($K_{Conv(c)}$) by the total number of vegetation pixels segmented in each pot ($GreenP_{(p)}$) at a given time point (*t*), as expressed in Eq. 4. The index (c) denotes the camera identifier and is retained to account for camera-specific calibration parameters (e.g., spatial conversion factor and geometric correction). Although each pot is observed by a single camera in the present experimental setup, this notation preserves consistency of the data structure and allows straightforward extension to multi-camera configurations.

$$Leaf\,Area_{(c,p,t)} = K_{Conv(c)} \cdot \sum GreenP_{(p)} \left[mm^2\right] \qquad \text{(Eq. 3)}$$

where $LeafArea_{(c,p,t)}$ is the estimated leaf area for camera (c), pot (p), and time (t); $KConv_{(c)}$ is the camera-specific spatial conversion factor (mm^2 per pixel); and sum $GreenP_{(p)}$ represents the total number of vegetation pixels identified within pot (p) at time (t).

Clusterization and counting

The output of the segmentation step formed the basis for identifying and counting individual plants. For each pot, all segmented green pixels ($GreenP_{(p)}$) were considered. A clustering algorithm was then applied to group adjacent blobs based on their spatial proximity: blobs whose maximum inter-pixel distance was less than 5 mm (e.g. ≈ 25 pixel) were aggregated into the same cluster. This procedure enabled the definition of cluster boundaries, which were then used to generate corresponding polygons ($Polyg_{(c,p,t)}$) *via* MATLAB's *polyshape* function. This function constructs two-dimensional polygons from vertex coordinates, yielding to a geometric representation of each aggregated (plant) cluster.

The estimation of germinated seedlings at a given time point was performed by analyzing these polygons in reverse temporal sequence. Starting from the latest acquisition, each segmented polygon was compared with those identified at earlier time points in the same area of the specific pot. A polygon was classified as a new emergence event if it did not spatially overlap with any polygon detected in preceding images. These non-overlapping polygons, defined as newly emerged polygons ($NE_{(c,p,t)}$), were then used to identify the timing of seedling emergence and subsequently characterize the germination dynamics.

This backward-tracking approach proved particularly effective during the later stages of the experiment, when growing seedlings tended to overlap, making it challenging to accurately delineate individual boundaries through image segmentation alone. Figure 1 illustrates an example of clustering outcome, where each polygon is shown in a different color. This visualization allows for the comparison of the same area across multiple time points. As the experiment progresses, clustering accuracy decreases due to increased overlap among seedlings. However, by tracing polygons backward in time, it is possible to return to an earlier development stage where clustering performs accurately, thus enabling accurate identification of both the position and the emergence time of each individual plant.

Automated counts obtained at the final time point were validated by comparing them with manual counts performed at the end of the experiment, validating the reliability and accuracy of the proposed method.

For clarity of presentation, two figures are provided: Figure 2 reports the pseudocode of the counting algorithm, and Figure 3 depicts the complete workflow summarizing all processing stages.

To evaluate the agreement between the automated counting algorithm and manual ground truth measurements, a correlation analysis was performed at two time points: an intermediate assessment conducted halfway through the experiment (midterm) and a final assessment performed at the end of the trial (final). For both evaluations, manual counts were considered as reference values, while automated counts were obtained using the proposed algorithm. The datasets were normalized as percentages with respect to the total number of samples for each replicate. Pearson's correlation coefficient was computed using the MATLAB *corr* function, together with the associated statistical significance (p-value), in order to assess the strength and reliability of the linear relationship between automated and manual measurements at both time points.

Results

Imaging system calibration

The calibration process produced binary masks for each camera, corresponding to the individual pots within its field of view. As shown in Figure 4b, the masks derived from a single camera are displayed using different colors for improved visual clarity. Beyond delineating the single pot regions, this procedure also enabled the estimation of the spatial

conversion factor, resulting in a mean value–of 0.19 mm^2 $pixel^{-1}$. This correspond to an equivalent linear spatial resolution (ground sampling distance, GSD) of approximately 0.44 mm $pixel^{-1}$. The computed coefficients varied by approximately 0.1% across all plots, a small difference that can be attributed to slight discrepancies in cameras elevation and alignment. The selected spatial resolution (< 0.5 mm $pixel^{-1}$) was not intended for fine morphological characterization, but rather to ensure robust segmentation and reliable separation of closely spaced seedlings, particularly under conditions of canopy overlap during later growth stages.

Image segmentation

The segmentation workflow proved to be effective in achieving the experimental objectives. Figure 5 illustrates a representative example of output from each step of processing. In the first stage (Figure 5a), geometric correction of the raw frame eliminated the barrel distortion and restored the true geometry of the scene.The gradient-based filter successfully removed borders areas where the green channel gradient exceeded the threshold, while preserving relevant plant structures, particularly the leaves (Figure 5b). In some cases, the central region of the seedling resulted to be excluded due to its narrow shape and the influence of surrounding background pixels, which caused it to be misclassified as a transition zone (Figure 5c). Despite this, the plant segmentation remained robust thanks to the 5 mm distance threshold applied during clustering.

Finally, Figure 5d shows the classification of the polygons generated with every segmented cluster represented with distinct colors for each individual pots. These polygons correspond to the final output of the analysis performed on a single image frame.

Clusterization and counting

The counting process was initiated from the most recent output and proceeded backward in time, iteratively incorporating the results from previous acquisitions up to the beginning of the experiment (i.e. first frame), enabling the identification of the precise moment of seedling emergence.

The clustering approach proved effective in restoring the geometric features of the segmented regions and accurately isolating individual seedlings, especially in early-stage frames where occlusion was minimal. However, as seedling size increased during later stages of

development, clustering occasionally merged multiple individuals into a single polygon. This limitation in results is visible in Figure 5d, where polygons are displayed with distinct color for replicate ID.

Nevertheless, by rewinding the temporal sequence allowed accurate determination of seedling emergence times and reliable counting even in conditions of extensive overlap. This approach demonstrated robustness even at suboptimal image resolution, such as those provided by low-cost cameras, which would otherwise hinder accurate segmentation and counting task.

The effectiveness of the method was validated by comparing automated counts at the final time point with manual counts performed at the end of the experiment after destructive harvest, based on a total of 294 seeds. As shown in Figure 6a, the automated results at the final time point yielded an RMSE of 1.12 and a coefficient of determination of $R^2 = 0.98$. In contrast, at the midterm evaluation, the method achieved improved performance, with $R^2 = 0.998$ and RMSE = 0.5. This difference can be attributed to the experimental conditions at the midterm stage, where fewer plants had germinated and individuals exhibited smaller sizes, resulting in reduced occlusion and simpler structural configurations, which in turn facilitated more accurate automated counting. The acquisition at the final time point was selected for validation because it represents both the standard endpoint in manual assessments and the most complex phase for image-based segmentation due to extensive overlap among seedlings.

The comparison between automated and manual counts showed an excellent agreement at both evaluation time points. For the final assessment, a Pearson correlation coefficient of R = 0.992 was obtained, with a highly significant *p*-value ($p=2.93 \times 10^{-10}$). Similarly, the midterm assessment yielded a correlation coefficient of R = 0.992, with a *p*-value of 1.93×10^{-15}. These results demonstrate a very strong linear relationship between the proposed automated method and the ground truth measurements, confirming the high accuracy and reliability of the developed counting algorithm throughout the experiment.Temporal alignment of the image sequences was also successfully achieved, as shown in Figure 6b, which presents an overlay of polygons obtained from different acquisition epochs. Early-stage polygons appear over later ones, representing the initial emergence events, while those from later stages progressively expand and merge due to plant growth and contact among

neighboring seedlings. This layering also confirms the spatial stability achieved through the central alignment marker.

As expected, the germination rate of the seeds was higher compared to those infected with *Rhizoctonia solani*. Moreover, the intra-treatment variability among replicates was significantly lower compared to the inoculated group, indicating a more uniform germination in the absence of the pathogen.

Growth vigor and counting

Data analysis revealed that the non-inoculated replicates consistently exhibited higher average vigor compared to those inoculated with the pathogen, in line with the initial expectations.

As shown in Figure 7a, the difference in germination percentage between inoculated and non-inoculated groups become evident and stable after approximately 80 h from sowing. Regardless of the treatment, the overall shape of the germination curve was similar for both groups, following a sigmoid trend, with most seeds germinating within 100 hours after sowing.

The germination data further support the impact of the pathogen, as inoculated seeds exhibited lower germination rates and greater variability among replicates compared to the non-inoculated controls. As expected, these results confirm that *Rhizoctonia solani* infection not only diminishes seed viability but also leads to inconsistent germination outcomes across experimental units.

The estimated seedling vigor curves illustrated in Figure 7b, reveals periodic fluctuations characterized by alternating peaks. These oscillations are likely linked to diurnal variations in leaf inclination and partial seedling closure during nighttime hours, as revealed by visual check into sample images.

In absolute terms, the inoculated replicates reached a leaf coverage of approximately 2000 mm^2, corresponding to about 7% of the pot surface area, whereas the non-inoculated replicates reached around 6000 mm^2, equivalent to roughly 20% of pot surface coverage. This substantial difference can be attributed to both the lower number of germinated seeds and the reduced vigor of seedlings grown in soil where the pathogen is present. The percentage of germinated seeds in the non-inoculated replicates exceeded 90%, while in those inoculated the germination rate was around 60%.

Discussion

Overall, the observed dynamics confirmed the trends identified in the analysis of seedling vigor. The inoculated replicates not only exhibited lower vigor and germination rates but also showed greater variability across samples. Indeed, these replicates were characterized by heterogeneous seedling emergence. Regarding vegetative vigor, the pathogen had a significant negative effect, reducing vigor by around 70% by the end of the experiment, and substantially limiting the vigor levels achieved by the emerged seedlings. Comparable systems have reported results in line with those obtained in this study. For instance, SeedGerm (Colmer *et al*., 2020) achieved a similar coefficient of determination for automatic number of emerged seedlings , despite employing higher-resolution cameras (8 MP HD USB cameras in its best configuration), compared to the 2.7 MP cameras used here. Additionally, the imaging setup of this study involved a greater camera-to-subject distance, monitoring a larger experimental area, resulting in a further lower spatial resolution. A noteworthy distinction of this study lies in the experimental conditions: here seeds were sown in a cultivation substrate, introducing additional complexity to the segmentation and counting process. In contrast, other approaches typically employ seeds on plates with high-contrast background, simplifying image analysis but providing less realistic conditions. The methodology adopted in this study offers a more realistic context for evaluating early plant development under biologically relevant conditions.

In comparison with the approach presented by Fuentes-Peñailillo (2023) where a deep-learning application based on SSD MobileNet was employed for crop detection in seedling trays, the method proposed in this study offers a different and complementary perspective. While their system allows real-time seedling detection through neural networks achieving accuracies ranging from 57% to 96%, depending on crop type and tray layout, it also highlights significant limitations related to environmental variability and dataset heterogeneity. These factors notably affected the generalizability of the model, underscoring the importance of both experimental setup and classification robustness. Conversely, the image-based pipeline developed in this study does not rely on deep learning models for real-time classification but instead leverages on temporal tracking of plant emergence and growth. By characterizing the germination kinetics and biomass development with high temporal resolution, the proposed method allows for a more detailed and accurate analysis of seedling

dynamics. Moreover, the consistent alignment and normalization steps contribute to minimizing variability across replicates, enhancing the reliability of automatic measurements. Although real-time prediction is not the primary objective of the study, the improved precision and interpretability of results make this approach particularly suitable for controlled experiments requiring high data spatial resolution.

Conclusions

The method for estimating the count of emerged seedlings and their vigour proved effective for achieving the objectives of the experiment, yielding highly accurate results in evaluating the kinetics of germination and growth of seedlings. This method is suitable to be applied in larger and more complex experimental designs involving multiple treatments, enabling accurate characterization of individual response. Notably, all acquired images were used for the analysis without the need for exclusion, demonstrating the robustness of the pipeline. Future developments will consider improving camera resolution while maintaining low overall costs, thanks to ongoing innovation in imaging hardware that is expected to facilitate such improvements.

In conclusion, the proposed methodology offers a practical and accessible solution for accurate in large germination and phenotyping experiment design both in greenhouse or in limited resources field applications.

References

Anandan A, Mahender A, Sah RP, Bose LK, Subudh, H, Meher J, et al., 2020. Non-destructive phenotyping for early seedling vigour in direct-seeded rice. Plant Methods 16:127.

Aydin MH, 2022. Rhizoctonia solani and Its Biological Control. Turk J Agric Res 9:118–135.

Chang KF, Hwang SF, Gossen BD, Turnbull GD, Wang H, Howard RJ, 2008. Effects of inoculum density, temperature, seeding depth, seeding date and fungicidal seed treatment on the impact of Rhizoctonia solani on lentil. Can J Plant Sci 88:799–809.

Chien CF, Lin TT, 2005. Non-destructive growth measurement of selected vegetable seedlings using orthogonal images. T ASABE 48:1953–1961.

Colmer J, O'Neill CM, Wells R, Bostrom A, Reynolds D, Websdale D, et al., 2020. SeedGerm: a cost - effective phenotyping platform for automated seed imaging and machine - learning based phenotypic analysis of crop seed germination. New Phytol 228:778–793.

Daami-Remadi M, Zammouri S, El Mahjoub M, 2008. Effect of the level of seed tuber infection by Rhizoctonia solani at planting on potato growth and disease severity. Afr J Plant Sci Biotechnol 2:34-38.

da Silva MP, Tylka GL, Munkvold GP, 2017. Seed treatment effects on maize seedlings coinfected with Rhizoctonia solani and Pratylenchus penetrans. Plant Dis 101:957–963.

Fuentes-Peñailillo F, Carrasco Silva G, Pérez Guzmán R, Burgos I, Ewertz F, 2023. Automating seedling counts in horticulture using computer vision and AI. Horticulturae 9:1134.

Gonzalez Garcia V, Portal Onco MA, Rubio Susan V, 2006. Review. Biology and systematics of the form genus Rhizoctonia. Span J Agric Res 4:55-79.

Gullino ML, Gilardi G, Garibaldi A, 2019. Ready-to-eat salad crops: a plant pathogen's heaven. Plant Dis 103:2153-2170.

Hwang SF, Ahmed HU, Turnbull GD, Gossen BD, Strelkov SE, 2014. The effect of seed size, seed treatment, seeding date and depth on Rhizoctonia seedling blight of canola. Can J Plant Sci 94:311–321.

Kumar KV, Reddy MS, Kloepper J, Lawrence KS, Yellareddygari S, Zhou XG, et al., 2011. Screening and selection of elite plant growth promoting rhizobacteria (PGPR) for suppression of Rhizoctonia solani and enhancement of rice seedling vigor. J Pure Appl Microbiol 5:641-651.

Losio MN, Pavoni E, Bilei S, Bertasi B, Bove D, Capuano F, et al., 2015. Microbiological survey of raw and ready-to-eat leafy green vegetables marketed in Italy. Int J Food Microbiol 210:88-91.

Olson E, 2011. AprilTag: A robust and flexible visual fiducial system. Proc. 2011 IEEE Int. Conf. on Robotics and Automation (ICRA), Shanghai. pp.3400-3407.

Patrignani A, Ochsner TE, 2015. Canopeo: a powerful new tool for measuring fractional green canopy cover. Agron J 107:2312–2320.

Raid RN, Sandoya-Miranda G, 2024. Diseases of lettuce. In: Elmer WH, McGrath M, McGovern RJ (eds.), Handbook of Vegetable and Herb Diseases. Handbook of Plant Disease Management. Cham, Springer; pp. 1-60.

Tomasi N, Pinton R, Dalla Costa L, Cortella G, Terzano R, Mimmo T, et al., 2015. New 'solutions' for floating cultivation system of ready-to-eat salad: A review. Trends Food Sci Technol 46:267-276.

Verwaaijen B, Wibberg D, Kröber M, Winkler A, Zrenner R, Bednarz H, et al., 2017. The Rhizoctonia solani AG1-IB (isolate 7/3/14) transcriptome during interaction with the host plant lettuce (Lactuca sativa L.). PLoS One 12:e0177278.

Wareing PW, Wang Z, Coley - Smith JR, Jeves TM, 1986. Fungal pathogens in rotted basal leaves of lettuce in Humberside and Lancashire with particular reference to Rhizoctonia solani. Plant Pathol 35:390-395.

Zhang Z, 2000. A flexible new technique for camera calibration. IEEE Trans Pattern Anal Mach Intell 22:1330–1334.

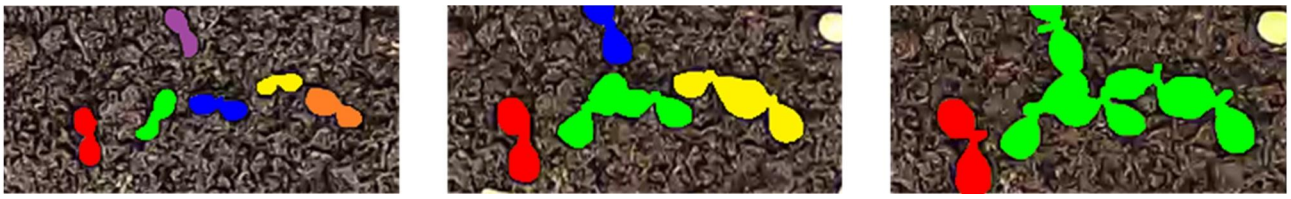

Figure 1. Example of the clustering process applied to a portion of the pot area. The three panels show the same region at different time points: 72 h, 120 h, and 150 h after sowing. Isolated clusters are color-coded, allowing visualization of how the segmentation and clustering results evolve over time as seedling overlap increases.

```
program COUNTSEEDLINGS (polygon_DB)
// Count the emerged seedlings from polygon dataset

(Nc, Nr, Nt) ← size (polygon_DB)
// Nt is the number of time points in the dataset
// Nr is the number of replicates for each treatment
// Nc is the number of cameras

for t = Nt to 1 step -1
    for r = 1 to Nr
        for c = 1 to Nc
            for ts = t to 1 step -1
                if  not polygon_overlap ( Polygon_DB [c][r][t], Polygon_DB [c][r][ts] ) then
                // check if the current polygon does not overlap with the previous time step polygons
                    valid_polyg [c][r][t]  ←  Polygon_DB [c][r][t]    // newly emerged plant
                    emerged_plant [c][r][t] ←  EmergedPlant [c][r][t] + 1
                    emersion_epoch [c][r][t] ←  ts

return valid_polyg,  emerged_plant, emersion_epoch
```

Figure 2. Pseudocode summarizing the main steps involved in the automated counting of germinated seedlings.

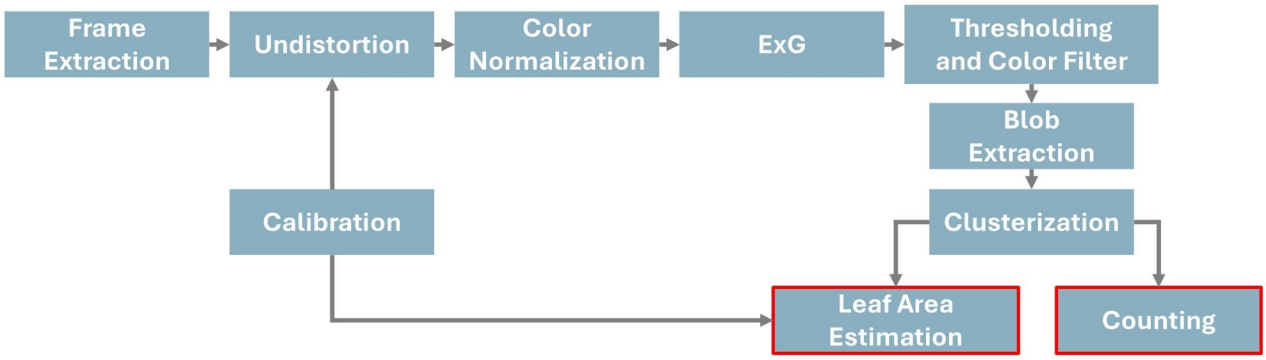

Figure 3. Flowchart of the image analysis and germination counting workflow. The diagram outlines the main processing steps performed by the algorithm, from image acquisition and pre-processing (including distortion correction and color normalization), to plant segmentation, clustering, and polygon extraction. The final stages involve temporal comparison across image sequences to identify newly seedling emergence events and compute germination counts over time.

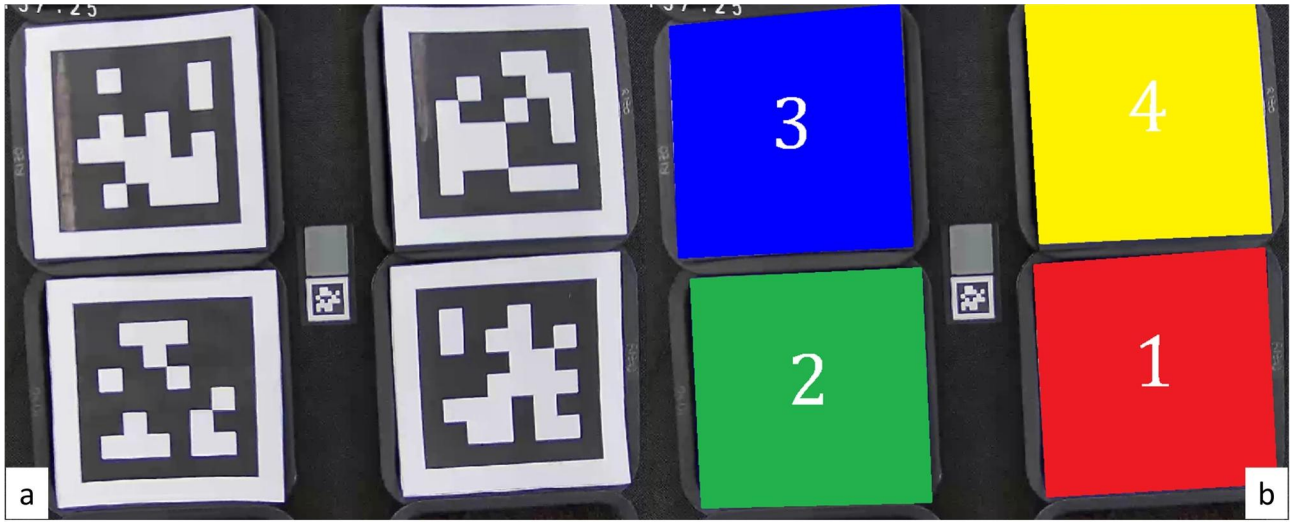

Figure 4. Example of the calibration process used to define the area assigned to each replicate within the image and to estimate the size of a single pixel. **a)** The calibration image displays the AprilTags used to delimit individual replicates. **b)** The overlay shows the corresponding binary masks in red, green, blue, and yellow.

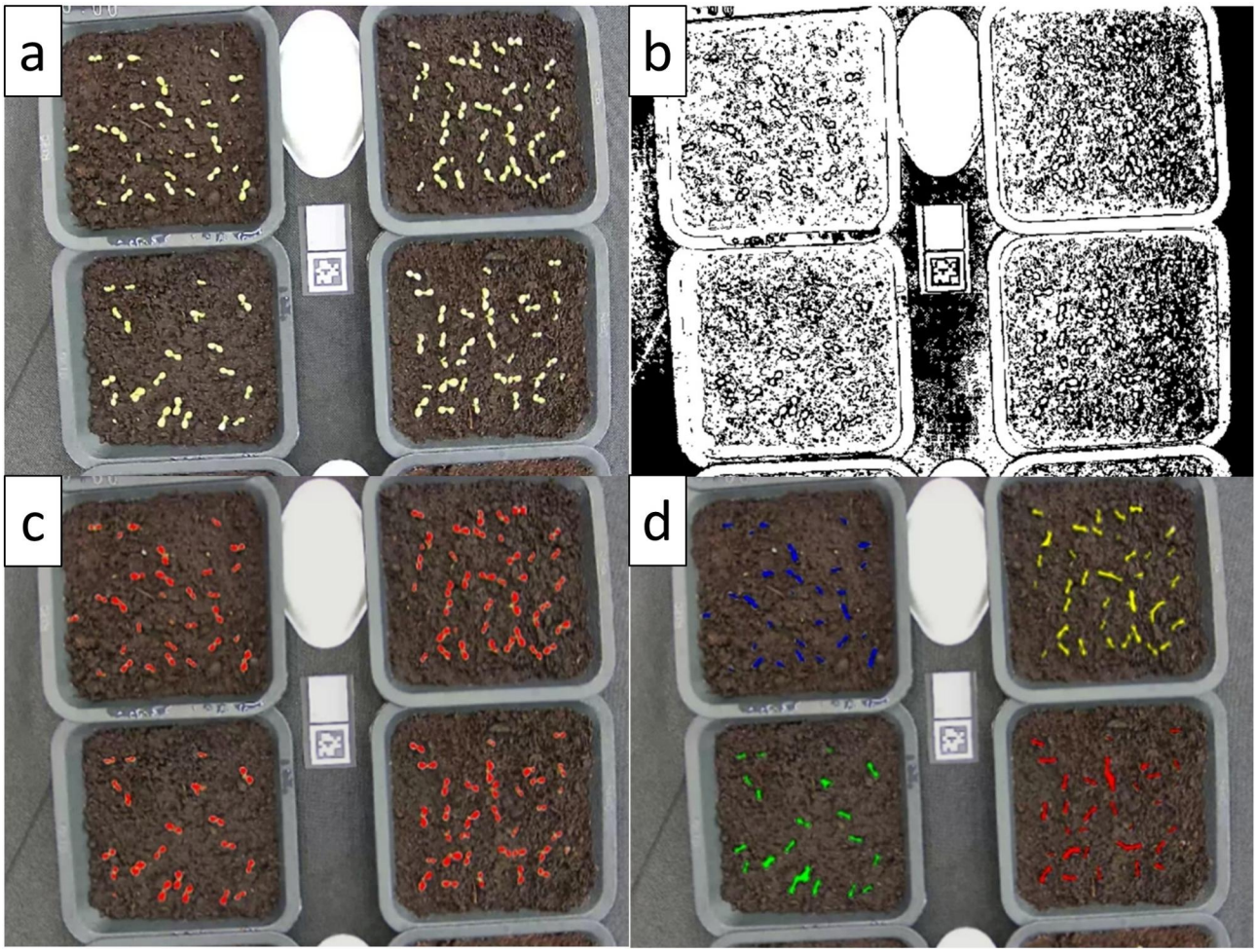

Figure 5. Segmentation workflow applied to a single video frame. **a)** Rectified image after undistortion, correcting for lens distortion and restoring geometric accuracy. **b)** Gradient-based filtering removes high-contrast transitions while preserving seedling features, especially the geometric features of the leaves. **c)** Example of blob segmentation. **d)** Result of the classification of segmented clusters and corresponding polygons, with each replicate area represented using a distinct color for clarity.

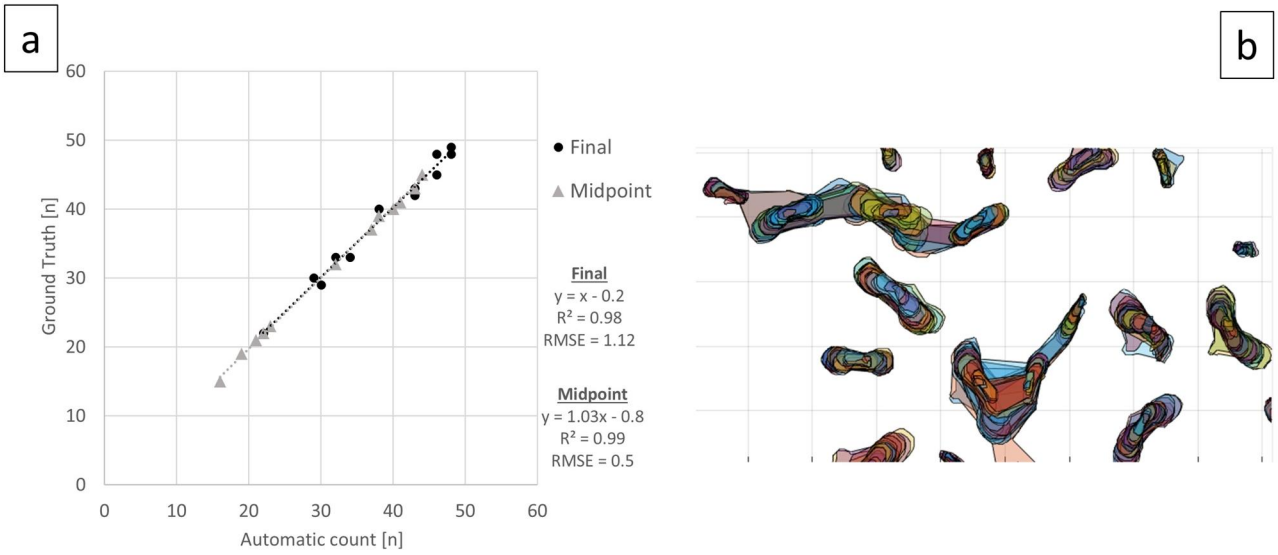

Figure 6. a) Validation results of the seedling counting method: the scatter plot shows the correlation between automated and manual counts at both evaluation time points; midterm results are reported in gray, while final time point results are shown in black; the plot includes the corresponding regression lines, R^2 values, and RMSE for each condition. **b)** Temporal overlay of the polygons extracted from a portion of a replicate during the experiment; the polygons are stacked chronologically, with the uppermost representing the earliest detections and the lower ones corresponding to later time points. The image highlights the high accuracy of the temporal alignment achieved throughout the monitoring process.

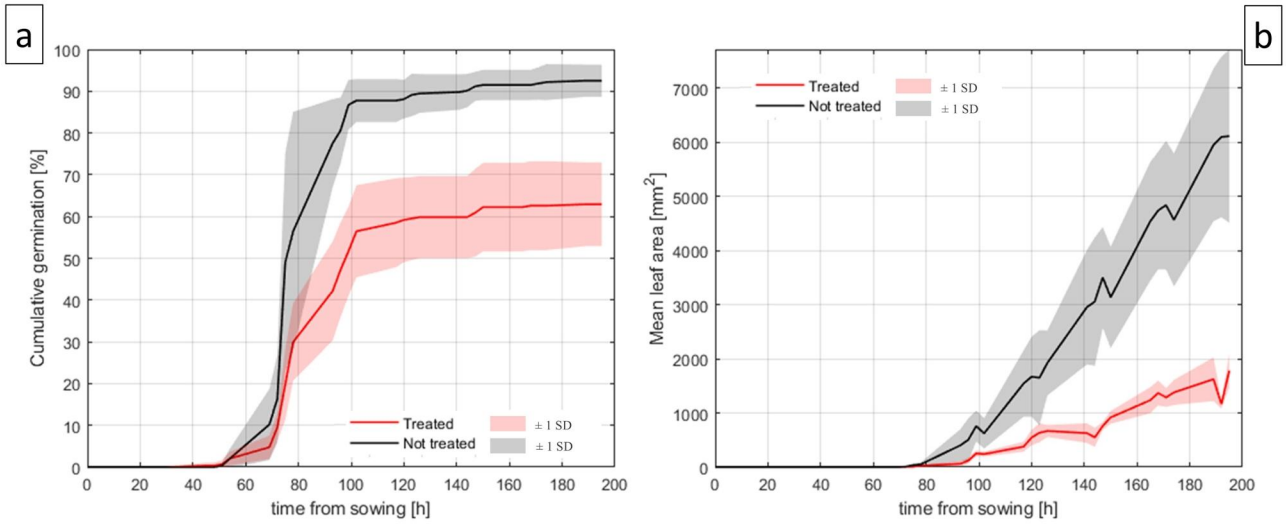

Figure 7. a) Time-course plot showing the number of germinated seedlings throughout the experiment, illustrating the emergence dynamics; the shaded area around the line represents the variability as ±1 SD. **b)** Biomass development dynamics over time, with the shaded region indicating ±1 SD around the mean values.